ARMA 19–1595

SAND2019-1954C

Permeability and deformation mechanisms during triaxial testing of early-age cement

Bauer, S.J., J. Wilson, E. N. Matteo, and G. Bettin

Sandia National Laboratories, Albuquerque, NM, USA,

ABSTRACT:

In wellbores, cement plays an important role in wellbore integrity. As wells age and are stressed during their life cycle, the cement sheath may deform, altering its permeability and, perhaps compromising its integrity. In this study, we use flow measurements (calculated permeability) to provide real-time insight into damage incurred during triaxial deformation of neat cement. Cracks may be induced during deformation and their linkage may be sensed in the flow measurements. Conversely, cracks and pores may be closed during deformation, arresting fluid flow.

We subjected room temperature specimens of neat Portland cement to confining pressures (0.7, 2.1, 13.8 MPa) and measured helium flow continuously during triaxial deformation. Axial displacement across a specimen was periodically halted to perhaps assure steady flow rate throughout the sample. We observed the apparent permeability to decrease from 5 to 4 to 0.2 μD with the imposed confining pressure increase. Each specimen, when subjected to differential stress, exhibited a slight decrease in apparent permeability, implying disconnects of flow paths. For the two lower confining pressures, apparent permeability began to increase just prior to macroscopic failure, suggesting microcrack linkage. For the 2.1 MPa confining pressure test, apparent permeability increased by a factor of five at macrofracture, and for the 0.7 MPa confining pressure test, apparent permeability increased by a factor of one hundred at macrofracture. At 13.8 MPa confining pressure, apparent permeability only decreases during triaxial loading, implying that poroelastic compaction restricts flow pathways and connectivity of appropriately oriented cracks for axial flow decreases during deformation. Failure by macrofracture did not occur in this sample.

Optical and scanning electron microscopy of deformed specimens indicate that pores and microcracks interact in complex manners, similar microcrack densities are observed in both 0.7 and 13.8 MPa test specimens, and pores represent both microcrack origination and localization sites. Larger pores (entrapped air voids) are sheared, flattened, and sites of crack opening. Micron-scale capillary porosity, determined using SEM image processing, is similar for all specimens.

The results from these few experiments indicate that microfracturing of cement during triaxial deformation results in permeability increases at low confining pressures. At the greater pressure, although microfracturing is observed, compaction and lack of microfracture interconnectivity have a greater effect on flow pathways, resulting in a permeability decrease during deformation.

1. INTRODUCTION

There are literally millions of boreholes in the continental US (both onshore and offshore) that include abandoned wellbores, production wellbores, and wellbores used during the operation of underground hydrocarbon storage. Some fraction is vulnerable to potentially catastrophic loss of wellbore seal integrity. The wellbore system consists of steel well-casing, cement, and rock. Cement represents a key seal component for the wells, and it used as a plug in the interior of the well-casing, as well as on the exterior of the casing as an annular cementitious sheath bonding the casing to the borehole rock. Well temperatures and pressures change with depth. Fluid injection and withdrawal will subsequently modify fluid pressures, temperatures, and local stress conditions. Over time, these fluctuations in conditions may induce fractures in the cement. The worst-case scenario might be the case where a negative feedback loop of damage and increased flow through the seal lead to catastrophic wellbore seal failure. It is plausible that the fractures create an increase of permeability/flow through the seal that, in turn, increase rates of chemical reactivity, which in turn leads further mechanical damage and so forth through the feedback loop. Damage to the cementitious sheath may provide potential leak paths for stored or produced product, and/or accessways for geoformation damaging fluids to possibly compromise casing integrity.

For many years, workers have evaluated the life cycle conditions of wells, with a view towards identifying critical material parameters and then tailoring cement properties to best survive for the life of a well. Because of the critical function of wells to satisfy energy production, storage, and environmental protection needs, many

aspects of cement sheath integrity have been studied experimentally, theoretically, and numerically [1-6]. Cracks and fractures that may form to allow fluids to access the cement and its bond to the casing are detrimental to well integrity. Mechanistic models have been developed and evaluated to show that loss of cement integrity depends on cement properties, well architecture, and well history [4].

Our work is focused on evolution of permeability of neat cement during deformation. We use permeability as a damage metric. We conduct triaxial experiments on the cement, and measure helium gas flow during those experiments to provide measures of real-time cement damage. The damage is later quantified through optical and scanning electron microscopy.

2. MATERIALS AND METHODS

The cement we studied is API Class G cement (Oilwell cement) with a water/cement ratio of 0.45. The cement was mixed and cast in tubes and were cured for three days at 50°C in water. The compressive strength is ~31.2 MPa (4525 psi) and the tensile strength (Split tension) is ~2.64 MPa (383 psi) [7]. Following curing, the outer diameter was ground to a finished cylinder near 3.81 cm, and then the ends were ground perpendicular to the diameter and parallel to each other to ASTM specifications; sample length is 7.62 cm. Each of the samples contained some visible cracks from the curing process, we believe that these cracks were not through-going and did not provide major flow pathways, nor did they necessarily predispose the samples to premature failure.

Thin section and SEM observations of the cement (discussed more below) exhibit at least two porosity scales. There are pores ~0.1 to ~0.3 mm diameter and round; these are probably air bubbles from when the cement was mixed. The capillary pores are ~1 to 5 microns in lengths and occur as space accommodating voids (generally not round).

2.1 Mechanical System

The mechanical portion of the test system consists of a triaxial cell in a 4.45 MN loading frame. The triaxial cell is capable of confining pressures to 200 MPa with sufficient axial force (stress) capabilities to fracture rock in compression/extension. A computer-controlled, servo-hydraulic testing system was used to conduct the axisymmetric tests at ambient temperature. The system consists of an MTS reaction load frame, coupled with a pressure vessel and loading column. Data collected in the experimental study included force, pressure, temperature, displacement, and volume change. Data are acquired using electronic transducers in which voltage is proportional to the change in the measured variable. In all cases, the constants of proportionality were determined through careful calibration using NIST traceable standards.

The test system has a pore fluid flow-through capability used to flow helium through the sample for permeability estimations.

We attempted to passively record microcracking events in the cement using acoustic emissions. The premise of seeking to detect acoustic emissions (AE) is simple. As the cement is deformed, fractures may form as stress is increased, generating acoustic waves (sound) [8, 9, 10]. The acoustic wave then travels omnidirectionally through the material, where it is sensed and recorded by an appropriate device.

The sensing devices are Dynasen CA1135 piezoelectric pins for AE transducers. The crystal itself is 0.05 in in diameter and 0.02 in thick and perform well at elevated temperatures and pressures available in the experimental load frames. The natural frequency is 2.5 MHz. The pins sense the p-wave and convert it to an analog electrical signal to be recorded after further processing by the rest of the AE system. A discriminator compares signals on multiple pins to determine whether an event occurred. The electrical output from events accumulates as voltage(s); 1 V corresponds to 1000 acoustic emission events. Four acoustic emission transducers were attached on opposing diameters near the specimen midheight. AE events are counted if similar magnitude and shape signals are triggered in at least three of the four transducers within a specified time window. We report cumulative AE events.

2.2 Permeability System

The permeability portion of the test system uses the technique described by [11] in which a helium mass spectrometer (a leak detector) is used to measure the downstream helium flow rate. The measurement system duplicates the classic Darcy's experiment with constant pressure differential and steady-state flow through a specimen. Once confining pressure has been applied to a specimen, an upstream pressure of ~0.21 MPa is applied to the upstream side of the sample. Soon afterwards vacuum pressure is applied to the downstream end of the sample, creating a vacuum downstream of the sample and allowing helium flow through the sample. A liquid nitrogen trap was located downstream of the sample, trapping water produced from the cement during the experiments. Using this method, μDarcy scale (10^{-18} m^2 on the low end), hydraulic permeability can be measured within a relatively short period of time. We estimate this

time to be on the order of a few minutes for the lowest permeabilities.

The helium leak detector (LD), which measures the flow rate of mass ^{4}He, is an Oerlikon Leibold Phoenix L300i, a specialized mass spectrometer which detects only ^{4}He. It works in the mass range of 2, 3, 4 amu, with a minimum detectable leak rate in vacuum mode of $<5x10^{-12}$ mbar l/s. Time constant of the leak rate signal is <1 s, and the filament is Iridium/Yttria-oxide. The analytical devices are semi-portable, located on a rolling cart so that all triaxial frames in the lab are accessible.

2.3 Observational Systems

Standard petrographic thin sections, 27x46 mm and 30 μm thickness, were prepared for each cement sample. Water was used to cut and polish the deformed cements. The orientation of each thin section relative to the loading direction and flow direction was noted for each sample. Thin sections were scanned using an HP ScanJet G4050 at 1200 dpi resolution to obtain an image of overall texture and macrofractures. Microtextural observations, photomicrographs, and microfracture density measurements were obtained using a Leitz Orthoplan transmitted light microscope. Microfracture densities were recorded at 609 points on a grid with 1 mm spacing. At each grid point, all microfractures that cross the horizontal crosshair when viewed at 16X magnification were counted, and the linear density calculated by dividing this number by the horizontal field of view of 1.0668 mm. Overall microfracture density was calculated by dividing the total number of microfractures observed by the total horizontal line length observed in each thin section.

Scanning electron microscopy (SEM) of each sample was performed using a TESCAN Vega3 SEM instrument. The thin sections were first coated with gold-palladium alloy using a Denton Vacuum Desk IV sputter-coater. Microtexture of each thin section was observed and imaged using backscattered electrons (BSE) and secondary electrons (SE) in high-vacuum mode at an accelerating voltage of 20.0 kV. Elemental composition from select portions of each thin section was obtained using an EDAX energy-dispersive (EDS) system at an accelerating voltage of 15.0 kV. EDS spectra were collected and analyzed using the TEAM EDS analysis system for the SEM.

Micron-scale capillary porosity was determined from ten BSE images at a range of magnifications (400X to 2.0kX) that show typical matrix texture with no fractures, large pores, or cataclastic material. In each image, white or gray pixels represent cement components and black pixels represents porosity. Using ImageJ software, each image was binarized so that all pixels are either white (solid material) or black (pore space). This processing step alone overpopulates the image with black pixels, so an adjustment to the gray-level threshold was made to achieve a visually satisfactory match between pore space in the original BSE image and that in the binarized image, a method also used by [12]. The proportion of black versus total pixels was calculated to represent the capillary porosity for that image area, which was then averaged for the ten images per sample to represent its capillary porosity.

3. EXPERIMENTAL SETUP

Jacketed and instrumented specimens were mounted onto the base of the pressure vessel and connected to pore-pressure feed-throughs in the pressure vessel. The pressure vessel was then assembled and placed into the reaction frame. The actuator in the base of the frame is raised gradually to bring the pressure vessel piston into contact with the reaction frame. The pressure vessel is then connected to the pressure intensifier and filled with Isopar®. At this point the servo-hydraulic control is turned on and data collection begins. The confining pressure is raised to the desired pressure, with the reaction frame actuator holding its position. The vacuum line and system was then connected to the flow-through pore pressure system. The confining pressure was maintained at test pressure while the specimen was subjected to upstream helium pore pressure, and downstream measurement of helium flow for 4-8 hours to obtain a baseline.

During the experiment, confining pressure is controlled, measured and tracked using a pressure transducer located in the intensifier connection line about a meter from the pressure vessel. Axial force is measured with a load cell external to the pressure vessel and O-ring friction is corrected for during data analysis. The specimen was shortened using a controlled displacement mode at a rate of approximately $8.1x10^{-6}$ cm/s. During loading, the advancement of the loading piston is periodically stopped and held for 15-30 minutes to observe potential changes in flow rate. During these hold times, it is observed that the load decreases. Force, displacement, confining pressure and gas flow were recorded in an automatic data acquisition/control system as a function of time.

Test specimens are instrumented to measure axial and radial displacements during application of the initial hydrostatic pressure, and during axial compression. (Figure 1). Displacement is measured with Linear Variable Differential Transformers (LVDTs) and/or

strain gages. LVDTs are mounted on the end caps to measure axial deformation, and in spring loaded rings placed near the sample midheight to measure change in diameter. The actuator has a separate LVDT that can be used as a backup for sample axial measurements. Sample mounted LVDTs are 0.254 cm full-scale. Displacement is used to calculate specimen strain, and stress is calculated using the measured force and updated cross sectional area based on lateral displacements during the experiments. Stain gages record strain directly.

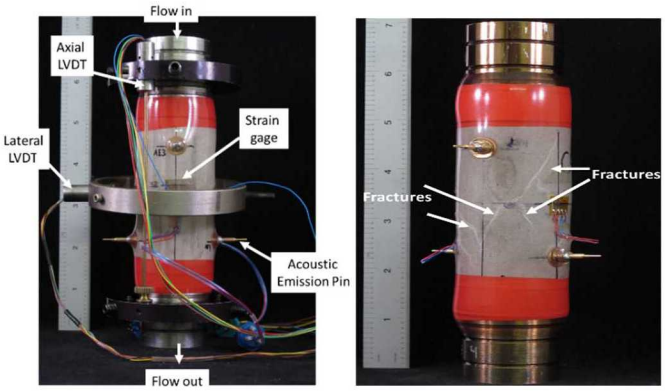

Figure 1. Left: Instrumented cement sample showing instrumentation, and Right: deformed sample (2.1 MPa test) showing post-test macro fractures.

To protect the vacuum system, low pressure (0.1- 0.2 MPa) relief valves, a fluid expansion tank, and a liquid nitrogen trap are part of the vacuum line system.

3.1 Permeability determinations

Permeability is calculated using [11] and is summarized in the following. Darcy's law is expressed as the measured flow rate of fluid crossing a unit area and is proportional to the pressure differential measured across the ends of the specimen. The permeability of the rock, k, is calculated by the following equation:

$$k_{app.}=Q_x \cdot \mu \cdot L /(A \cdot \Delta P) \quad (1)$$

where k_{app} is the apparent permeability (Darcy), Q_x is the flow rate in the axial direction of the specimen (cm^3/s), μ is the viscosity of flowing helium (cP), ΔP is the pressure differential measured across the ends of the specimen (atm), L is the length of the specimen (cm), and, A is the cross-sectional area (cm^2) perpendicular to the axis of the specimen. The viscosity of the helium at 25°C temperature used in this study is 0.196 cP [11]

Darcy's law, equation (1) assumes an incompressible medium. For the compressible helium, the volumetric flow rate Q varies with pressure from one face of the specimen to the other. Since we assume that the downstream pressure is close to zero due to vacuum condition, equation (1) can be modified for a compressible fluid such as helium:

$$k_{He} = 2\, Q_{in} \cdot \mu \cdot L/(A \cdot \Delta P) \quad (2)$$

where k_{He} is the permeability measured using helium and Q_{in} is the volumetric flow rate in the inlet side of the specimen. Thus, using the equation of state of the gas under constant temperature, k_{He} is related to the apparent permeability (k_{app}) based on incompressible fluid as follows:

$$k_{He} = 2\, k_{app.}\, Q_{in}/Q_{ref} = 2\, k_{app.}\, P_{ref}/P_{in} \quad (3)$$

where P_{ref} is the reference pressure, Q_{ref} is measured, and P_{in} is the pressure on the inlet side.

The permeabilities calculated above using Darcy's law need to be corrected for gas "slippage", which is an apparent increase in flow rate observed when the pore space approaches the mean free path of the gas; this is the well-known Klinkenberg factor [13], which is especially important for low permeability materials and low mean gas pressures.

The equation relating the liquid permeability to the gas (Helium) permeability is

$$k_{He} = k_{liq}\,(1 + b_{He}/P_{bar}) \quad (4)$$

where k_{He} is the permeability to helium, k_{liq} is the permeability to liquid, b is the Klinkenberg coefficient, and P_{bar} is the average pressure in the test section.

The Klinkenberg coefficient for air has been correlated to the liquid permeability [14] using numerous samples from oil-field cores and can be written as follows

$$b_{air} = 0.11\, k_{liq}^{-0.39} \quad (5)$$

where b_{air} is the Klinkenberg coefficient for air in pascals, and k_{liq} is in m^2. Note that the permeability data used in this correlation has a minimum value of about 10^{-17} m^2, which is much higher than the present data. Subsequently, permeabilities were measured on low-permeability gas sands down to approximately 10^{-19} m^2 [15]; their correlation is

$$b_{air} = k_{liq}^{-0.33} \quad (6)$$

They compared their data with the correlation from [14] and showed that the correlation gives reasonable results down to their lowest permeability value. Because the [15] correlation used lower permeability data, it will be used in this evaluation. In addition, their correlation results in a smaller Klinkenberg correction than [14] for the present data set. The Klinkenberg factor given above needs to be

corrected for the gas used as the permeant, which is helium in this study. As given by [16], the correction equation is

$$b_{He}=b_{air}\mu_{He}/\mu_{air}(T_{He}/298.15K)^{1/2}(28.97/m_{He})^{1/2} \quad (7)$$

or a factor of 2.9 in this study.

The [15] correlation has been extrapolated to lower permeabilities in this evaluation assuming that "slip" flow occurs, which can be modeled by the Klinkenberg correlation. However, at very low permeabilities, other diffusion mechanisms become important such as configurational diffusion [17]. In configurational diffusion, the pore size is approximately equal to the size of the gas molecules, and the configuration of the molecules and molecule-surface effects become important. The permeability drops off drastically in the configurational diffusion range. Based on simple calculations, the transition between "slip" flow and configurational diffusion is of the order of 10^{-21} m^2 or 10^{-9} Darcy. Therefore, the applicability of the above Klinkenberg correction is limited to liquid permeabilities of 10^{-9} Darcy and greater. Permeabilities for other (heavier) gases and liquids are much lower than those reported herein. We calculate apparent and helium permeabilities, and the Klinkenberg correction; liquid permeabilities are likely ~2 orders of magnitude lower.

4. EXPERIMENTAL RESULTS

Here we report data from three experiments, one each at 0.7, 2.1, and at 13.8 MPa confining pressure. These pressures were chosen to begin to study/explore cement permeability versus deformation relationships for a range of conditions.

Mechanical test information is presented in Table 1 and Figures 2, 3, 4, and 5. In Figure 2 A, B, differential stress versus axial strain and cumulative acoustic emissions versus axial strain for cement tested at 2.1 MPa and 13.8 MPa confining pressure are presented (the 0.7 MPa test had poor AE data). The high axial strain for the 13.8 MPa test may be applicable to severe-deformation well conditions for example when casings are not concentric to the borehole. At 2.1 MPa confining pressure, the AE accumulation is episodic, with three jumps to the maximum of ~70 counts. At 13.8 MPa confining pressure, the AE accumulation is again episodic for the entire loading interval. We note that about the same number of AEs is observed in both tests at about 0.015 axial strain.

Table 1. Triaxial strength and axial strain at test end

Confining Pressure (MPa)	Ultimate strength (MPa)	Axial Strain at test end
0.7	35	0.007
2.1	58	0.015
13.8	55	0.13

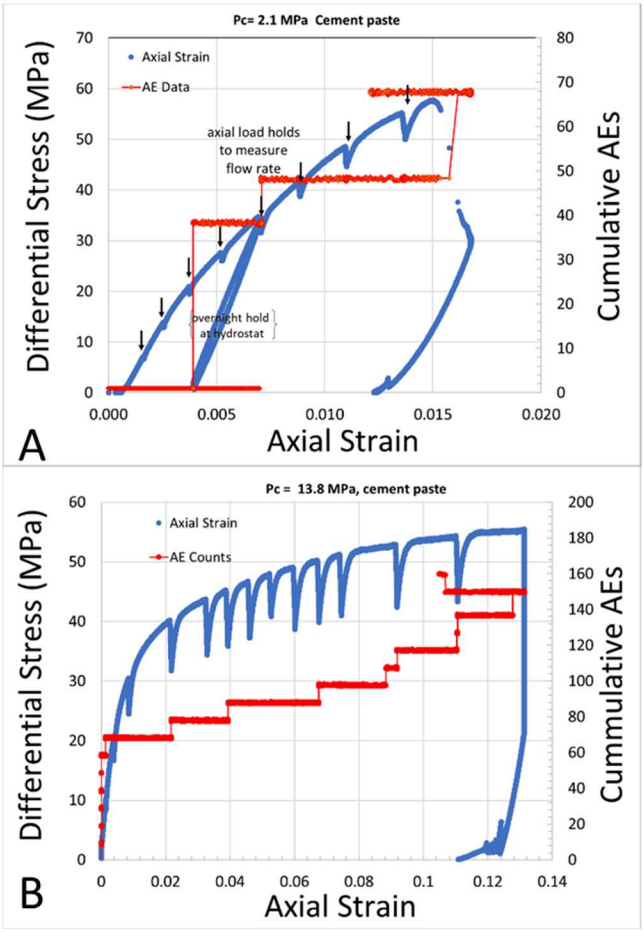

Figure 2. A. Differential stress versus axial strain and cumulative acoustic emissions versus axial strain for cement tested at 2.1 MPa confining pressure. B. Differential stress versus axial strain and cumulative acoustic emissions versus axial strain for cement tested at 13.8 MPa confining pressure.

Loading stops were used in all tests to make prolonged flow measurements and are indicated by the black arrows in each figure. The strength is least at the lowest (0.7 MPa) confining pressure, with an abrupt specimen failure

by load loss at less than .01 axial strain (Figure 3A). With a small increase to 2.1 MPa confining pressure, the strength increases to 58 MPa, with a near doubling of strain at failure (Figure 3B). At the greatest confining pressure (13.8 MPa), the cement work hardens until the test was ended at near 0.13 axial strain (Figure 3C). The apparent permeabilities determined as a function of axial strain are presented in Table 2 and Figure 3. Apparent permeability (K_{app}) at hydrostatic conditions decreases with increasing confining pressure (Table 2). For all confining pressures studied, K_{app} decreases slightly from the start of loading to about mid point in each test. At the end of loading, for the two lower confinng pressures, K_{app} increases dramatically, coincident with the deveopment of presumed macrofractures (stress drop). At 13.8 MPa confining pressure, K_{app} continues to decrease slightly for the entire loading period. At the end of all tests, upon unloading, K_{app} increases for all tests, perhaps reflecting fracture opening.

Table 2. Permeability determinations

Confining pressure (MPa)	K_{app}/K_{He} prior to axial loading µD	K_{app}/K_{He} mid axial loading µD	K_{app}/K_{He} end axial loading µD	K_{app}/K_{He} end of test µD
0.7	5.9/4.0	5.0/3.7	113/76	270/167
2.1	4.3/3.0	3.3/2.3	11.6/8.1	12.0/8.4
13.8	0.24/0.17	0.17/0.12	0.16/0.11	0.20/0.14

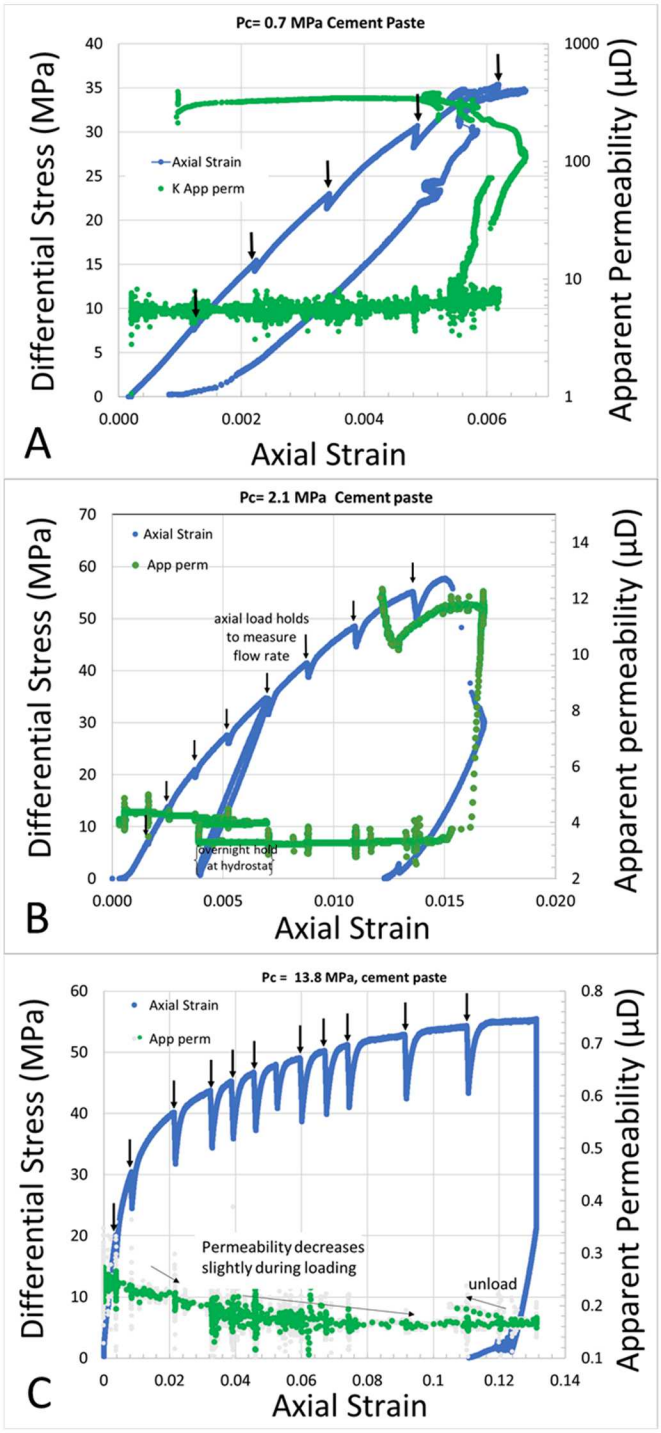

Figure 3. Differential stress versus axial strain and apparent permeability versus axial strain for cement tested at A. 0.7 MPa, B. 2.1 MPa, C. 13.8 MPa confining pressure.

5. OBSERVATIONS

The observed textural elements and deformational elements present include the initial cement paste texture, large microfractures (more than a few mm in length), small microfractures, entrapped air voids that are ~0.1 to ~0.3 mm diameter and round, and capillary pores that are ~1-5 microns in lengths and occur as space accommodating voids (generally not round).

The capillary porosity values we determine for all post-test samples are in the range of 12 to 16%. These are consistent with porosity values of similar cement pastes determined through SEM image analysis [17, 18], and they do not vary with changes in confining pressure, apparent permeability, or strain.

While we observed cracks in the samples from fabrication/curing, we believe that these cracks were not through-going and did not provide major flow pathways (the permeability of all samples is low/appropriate for the confining pressure tested), nor did they necessarily predispose the samples to failure (the strengths are consistent with published values).

Microfracture linear crack densities range from 0.08 to 0.29 mf/mm and show no apparent relationship to test confining pressure or total sample strain. With increasing confining pressure, macrofractures tend to increase in angle to load direction.

At the millimeter scale, large pores, which are entrapped air voids interact with and are involved in the microfracturing process. Typically, these voids form when the cement has not been vibrated or tamped enough to remove air before the initial solidification. These large pores are observed to shear with cataclasis and comminution along fracture surfaces (Figure 4A) and pores interact with each other, localizing deformation as they flatten, shear and facilitate crack growth (Figure 4B).

Large pores (air voids) are also observed to crush/flatten at various stages, exhibiting aspects of borehole breakouts with flattening perpendicular to loading, sloughing and microfractures appearing to originate from pores (Figure 4 C, D).

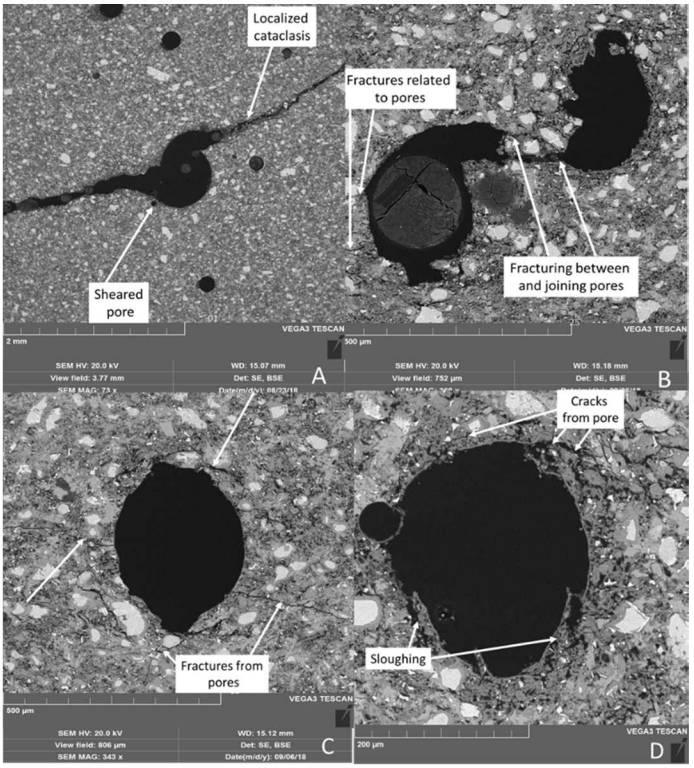

Figure 4. A. Sheared air void with cataclasis (Pc= 13.8 MPa); B. Interacting pores (air voids). C. Flattened air void pore with fractures (Pc= 2.1 MPa); D. Sloughing from air void and cracks from air void (Pc= 2.1 MPa). Loading direction is horizontal in all images.

At the micron scale (Figure 5A), we observe a skeletal matrix of calcium-silicate-hydrate (C-S-H)with unhydrated cement grains and capillary pores[20]. Microfractures crosscut the groundmass and the cement grains, connecting previously isolated capillary pores (Figure 5B). In the sample subjected to the highest confining pressure, we also observe some large-aperture microfractures, which contain Si-rich cataclastic material with some larger grains incorporated. The cement matrix directly adjacent is variably microfractured, but is otherwise undisturbed (Figure 5 C, D).

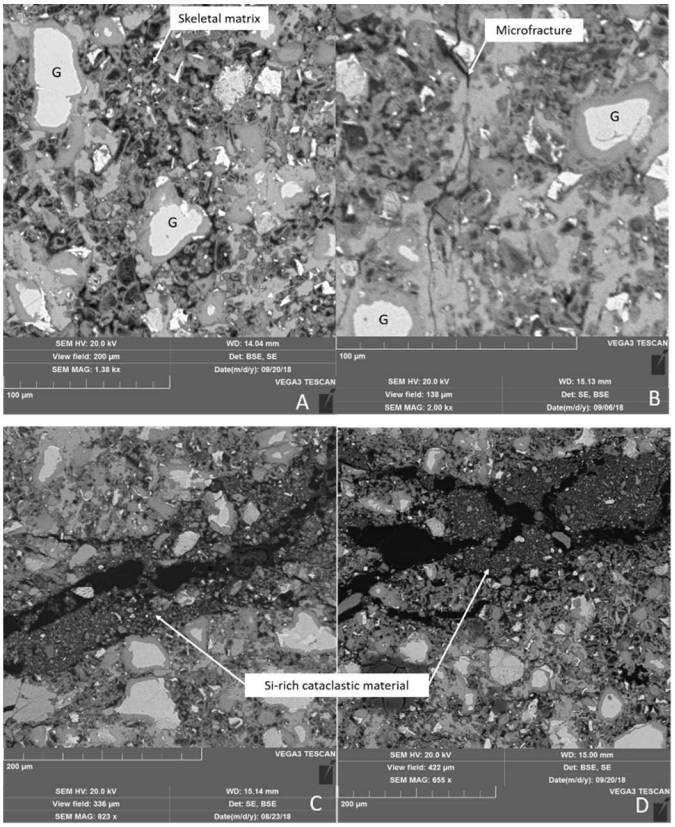

Figure 5. A, B, Examples of skeletal matrix, cement components, and their interactions with microfractures (G=unhydrated cement grains). C, D Examples of large-aperture microfractures with Si-rich, cataclastic material. Loading direction is horizontal in all images.

6. DISCUSSION OF RESULTS AND CONCLUSIONS

We present results of real-time measurements indictive of microstructural changes during deformation of neat cement during triaxial experiments conducted at room temperature. The discussion and conclusions with respect to cement material properties for wells at depth are presented and predicated considering the limited number of experiments conducted (three), and that the young paste is more ductile owing to its early-age strength. The signal of microstructural evolution is changes in helium flow rate for the imposed stress/strain state. From those flow measurements we infer permeability. Using optical and scanning electron microscopy, end-of-test images provide valuable snapshots of pore structure and operative deformation mechanisms.

The strength at 0.7 MPa is consistent with previous characterization [7]. The strength of neat cement increases with increasing confining pressure. Macroscopically the cement fractures at the two lower confining pressures and tends to strain harden at the greatest confining pressure.

The observed deformation mode change implies that macrofracture formation from compressive processes like those of the tests performed may be an issue in wells at shallow depths or situations where locally low effective confining pressures are present. For example, high formation pore pressures could cause low effective confining pressures in the cement. Incomplete cement jobs leave gaps in cement continuity and create free surfaces, reducing the effective confinement. At the greatest confining pressure, the cement work hardens, the strains are permanent at test end. Permanent strains may be inconsequential in monotonically stressed well cement. If, however, wells are stress cycled, the cements or cement-steel/rock interfaces may open from extensile cracking upon unloading.

Acoustic emissions provide some information of microstructural modifications, but the limited data set does not allow us to directly relate them to K_{app} changes. Some of the AEs reflect pore collapse as well as microfracture formation. For both confining pressures, the AEs may reflect similar phenomenon, pore collapse, shearing and new crack formation, however they manifest differently at the different confining pressures.

K_{app} for neat cement is in the μD range, consistent with previous workers [21]. Consistent with conventional wisdom, K_{app} decreases with increasing confining pressure, implying that cracks close and pores are diminished in volume with increasing confining pressure. For the two lower confining pressure tests, K_{app} decreases then increases prior to load loss and macrofracture, implying that flow paths are choked slightly during initial axial loading, and then favorably oriented-to-flow microcracks begin to open and connect. At and near macrofracture, the macrofracture flow path dominates measured flow. For 13.8 MPa confining pressure, permeability only decreases implying compaction processes dominate throughout the deformation.

Entrapped air voids and capillary pores are each involved in the deformation as sources of microfractures. The observations of crack development and crack existence at test end support observations of permeabilty development during triaxial deformation. The large microfractures created at low confining pressures provide ample flow paths for the large increase in K_{app} observed. However, the number of smaller microfractures and the capillary porosity calculated within the skeletal matrix and cement grains do not reveal microstructural differences between the highest and lowest pressures. This may be due to the presence of the larger (0.1 to 0.3 mm diameter) pores (air voids) accommodating strain through pore collapse and related microfracturing. These features were not quantified due to the difficulty in statistically capturing the larger pores and related microfractures at the thin section scale. We feel that more work is warranted to better relate the lab measurements to the observations at the larger pore scale.

6. ACKNOWLEDGEMENTS

The authors would like to thank Dr. Moneeb Genedy at the University of New Mexico for mixing and curing the cement samples. This paper describes objective technical results and analysis. Any subjective views or opinions that might be expressed in the paper do not necessarily represent the views of the U.S. Department of Energy or the United States Government. Sandia National Laboratories is a multi-mission laboratory managed and operated by National Technology and Engineering Solutions of Sandia, LLC., a wholly owned subsidiary of Honeywell International, Inc., for the U.S. Department of Energy's National Nuclear Security Administration under contract DE-NA0003525.

7. REFERENCES

1. M. B. Dusseault, Gray, M. N., Nawrocki, P. A., (2000) Why Oilwells Leak: Cement Behavior and Long-Term Consequences (paper presented at the International Oil and Gas Conference and Exhibition, SPE, China.
2. M. Zhang and S. Bachu (2011) Review of Integrity of Existing Wells in Relation to CO2 Geological Storage: What Do We Know? International Journal of Greenhouse Gas Control 5, no. 4.
3. A-P. Bois, M-H. Vua, S. Ghabezloo, J. Sulem, A. Garnier, Jean-Benoît Laudet, (2013) Cement sheath integrity for CO2 storage – An integrated perspective, Energy Procedia 37 (2013) 5628 – 5641, doi:10.1016/j.egypro.2013.06.485
4. A.-P. Bois, Garnier, A., Galdiolo, G., and Laudet, J.-B. (2012) Using a Mechanistic Model to Forcast Cement-Sheath Integrity. SPE Drilling & Completion, 303 – 314.
5. S.P. Gomez, S. R. Sobolik, E. N. Matteo, M. R. Taha, and J. C. Stormont, (2017) Investigation of wellbore microannulus permeability under stress via experimental wellbore mock-up and finite element modeling. Computers and Geotechnics 83 168-177.
6. J.C. Stormont, S. G. Fernandez, M. R. Taha, and E. N. Matteo, (2018) Gas flow through cement-casing microannuli under varying stress conditions. Geomechanics for Energy and the Environment 13, 1-13.
7. M. Genedy, (2019) personal communication
8. D. Lockner, (1993) The role of acoustic emission in the study of rock fracture, International Journal of Rock Mechanics and Mining Sciences & Geomechanics Abstracts, Volume 30, Issue 7, p. 883-899; doi.org/10.1016/0148-9062(93)90041-B.
9. S.J.D Cox, and Meredith, P.G. (2014) Microcrack formation and material softening in rock measured by monitoring acoustic emissions. International Journal of Rock Mechanics and Mining Sciences & Geomechanics Abstracts, 30(1), 11-24.
10. Moradian, Z., Einstein, H.H. and Ballivy, G. (2016) Detection of Cracking Levels in Brittle Rocks by Parametric Analysis of the Acoustic Emission Signals. Rock Mechanics and Rock Engineering, 49(3), 785-800.
11. M. Y. Lee and S. J. Bauer (2016) Development of Helium-Mass-Spectrometry-Permeameter for the Measurement of Permeability of Near-Impermeable Rock ISSN 0723-2632 Rock Mech Rock Eng DOI 10.1007/s00603-016-1058-1.
12. D. A Lange, H. M. Jennings, and S.P. Shah (1994) Image analysis techniques for characterization of pore structure of cement-based materials, Cement and Concrete Research 24 (5), 841-853.
13. L. J. Klinkenberg, (1941) The permeability of porous media to liquids and gases, API Drilling and Production Practice, 200-213.
14. J. G. Heid, J.J. McMahon, R. F. Nielson, and S. T. Yuster, (1950) Study of the permeability of rocks to homogeneous fluids," API Drilling and Production Practice, 230-244, 1950.
15. F. O. Jones, and W. W. Owens, (1980) A laboratory study of low-permeability gas sands, J. Petroleum Technology, 1631-1640.
16. S. W. Webb, (1996) Gas-phase diffusion in porous media – evaluation of an advective-dispersive formulation and the Dusty-Gas model including comparison to data for binary mixtures," SAND96-1197, Sandia National Laboratories, Albuquerque, New Mexico.
17. J. Xiao, and J. Wei, (1992) Diffusion mechanism of hydrocarbons in Zeolites – I. Theory, Chemical Engineering Science, 47, 1123-1141.
18. J. E. Ash, M.G. Hall, J. I. Langford, and M. Mellas, (1993) Estimations of degree of hydrations of Portland cement pastes, Cement and Concrete Research 23, 399-406.
19. E. Gallucci, X. Zhang, and K.L. Scrivener (2013) Effect of temperature on the microstructure of calcium silicate hydrate (C-S-H), Cement and Concrete Research 53, 185-195.
20. J. J. Thomas, H.M. Jennings, and J.J. Chen, (2009) Influence of Nucleation Seeding on the Hydration Mechanisms of Tricalcium Silicate and Cement, The Journal of Physical Chemistry C 113 (11), 4327-4334, DOI:10.1021/jp809811w.
21. X. Yang, E. Kuru, M. Gingras, S. Iremonger, (2019) CT-CFD integrated investigation into porosity and permeability of neat early-age well cement at downhole condition, Construction and Building Materials, DOI: 10.1016/j.conbuildmat.2019.02.004